



Surface amending effect of N-doped carbon-embedded NiO films for multirole electrochromic energy-storage devices

Kue-Ho Kim^a, Seock-Joon Jeong^a, Bon-Ryul Koo^b, Hyo-Jin Ahn^{a,b,*}

^a Department of Materials Science and Engineering, Seoul National University of Science and Technology, Seoul 01811, Republic of Korea

^b Program of Materials Science & Engineering, Convergence Institute of Biomedical Engineering and Biomaterials, Seoul National University of Science and Technology, Seoul 01811, Republic of Korea



ARTICLE INFO

Keywords:

Nickel oxide films
Multirole electrodes
N-doped carbon
Electrical properties
Sol-gel method

ABSTRACT

We synthesize N-doped carbon-embedded porous NiO electrodes using an amide-condensation reaction assisted sol-gel method for multirole electrochromic (EC) energy-storage devices. By adjusting the amount of oleylamine added to the sol solution, we simultaneously developed N-doped carbon-embedded NiO films with an optimized surface pore structure. NiO films fabricated using 2.5 wt% oleylamine (2.5OL-NiO) exhibited superior EC energy-storage performance outcomes, specifically with regard to the switching speed (coloration speed of 3.2 s and bleaching speed of 2.7 s), coloration efficiency (CE) value (48.5 cm²/C), and the specific capacitance (235.8 F/g at a current density of 2 A/g). These attractive EC energy-storage performance outcomes are primarily due to the enhanced electrochemical activity with the optimized surface pore structure. This porous film morphology was developed using evaporated H₂O molecules generated from an amide condensation reaction. A second cause was the improved electrical conductivity due to the highly conductive N-doped carbon formed by means of multimeric amide condensation, which provides preferred electron pathways. Accordingly, we believe that our results present a promising electrode design strategy by which to realize multirole EC energy-storage devices.

1. Introduction

Due to the increase in global energy consumption, many researchers around the world are currently seeking novel energy-saving strategies to achieve high energy efficiency accompanied by long device lifetimes [1–3]. In this regard, electrochromic (EC) devices have received considerable attention since their discovery given their use of smart windows capable of adjusting based on the level of sunlight flux, thus reducing energy consumption by as much as 40% [3–5]. In addition, EC devices have been applied to electronic displays, electrochromic mirrors, and outdoor billboards with several advantageous characteristics, including their color variation capabilities, transmittance in the visible region, and low operating voltages [6,7]. Recently, EC devices with good energy-storage performance capabilities due to their use of the pseudocapacitance generated during an EC redox reaction have been reported, a development that can broadly expand their applications. These multirole EC energy-storage devices offer color variations with an energy-storage function simultaneously and are therefore capable of monitoring the energy-storage state via their color variation [8]. Generally, such devices are composed of functional layers, typically two

transparent conductive layers, anodic and cathodic reaction layers, and an ionic conductive layer [9,10]. In addition, most multirole EC energy-storage performance metrics (transmittance modulation, switching speeds, coloration efficiency (CE), and specific capacitance) are mainly attributed to the anodic and cathodic reaction layer. Various materials, such as transition metal oxides, conjugated polymers, and organic molecules, have been investigated to determine their ability to exhibit EC properties and additional energy-storage capabilities [11,12]. Among transition metal oxides, NiO films have attracted a considerable amount of attention as an anodic EC layer due to their high electrochromic efficiency, compatibility with cathodic WO₃ EC layers, low material costs, and potential use as an energy-storage electrode [13,14]. The color of NiO films can change from pale yellow to deep brown when voltage is applied, and this electrochromism is related to the oxidation number variation of nickel from Ni²⁺ in the bleached state to Ni³⁺ in a colored state [15].

However, to apply NiO films to practical EC energy-storage applications, a low CE value (20–40 cm²/C), slow switching speeds (8–15 s), and low specific capacitance (< 180 F/g) remain as key factors to be addressed [16,17]. To overcome these limitations, it is important to

* Corresponding author at: Department of Materials Science and Engineering, Seoul National University of Science and Technology, Seoul 01811, Republic of Korea.

E-mail address: hjahn@seoultech.ac.kr (H.-J. Ahn).

<https://doi.org/10.1016/j.apsusc.2020.147902>

Received 2 July 2020; Received in revised form 9 September 2020; Accepted 13 September 2020

Available online 17 September 2020

0169-4332/ © 2020 Elsevier B.V. All rights reserved.

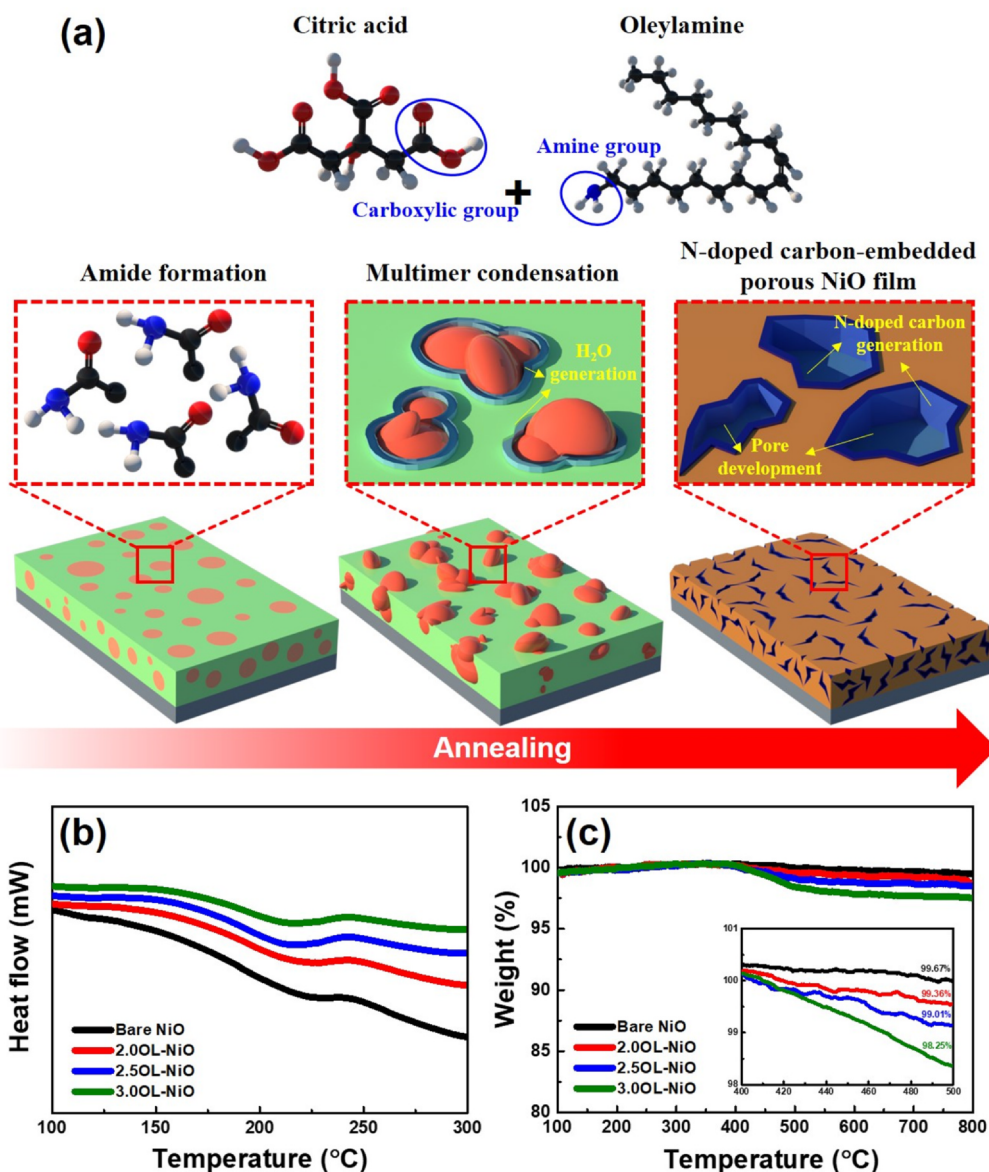


Fig. 1. (a) Schematic illustration of the simultaneous synthetic procedure used to create N-doped carbon-embedded porous NiO films, (b) DSC curves of the solution of the bare NiO, 2.0OL-NiO, 2.5OL-NiO, and 3.0OL-NiO samples from 100 to 300 °C in air, and (c) TGA curves of bare NiO, 2.0OL-NiO, 2.5OL-NiO, and 3.0OL-NiO samples from 100 to 800 °C in air.

facilitate the electrochemical activity and electrical conductivity of NiO films, as doing so will directly influence the EC energy-storage performance outcomes. At this point, studies focusing on surface conditions, such as pore development and dimension adjustments, are well known as strategies that enhance the electrochemical activity of transition metal oxides [18]. Moreover, electrical conductivity improvements can be achieved through metal ion doping or by constructing a composite structure with highly conductive materials [19–21]. Xia et al. demonstrated porous NiO thin films with reaction activity enhanced by means of chemical bath deposition, demonstrating an optimized CE of 42 cm²/C at 550 nm and improved switching speeds (8 s for coloration and 10 s for the bleaching speed) [22]. Chen et al. fabricated porous NiO nanoflake bifunctional electrodes that showed high CE values of 63.2 cm²/C at 632.8 nm and capacitance of 74.8 mF/cm² due to their accelerated electrochemical activity [23]. In addition, Zhang et al. fabricated Co-doped NiO nanoflake arrays with outstanding EC performance capabilities, including a high transmittance modulation rate (88.3%), a high CE value (47.7 cm²/C), and rapid switching speeds (3.4 s for coloration and 10 s for the bleaching speed) [17]. However,

despite these efforts, the multirole EC energy-storage performance capabilities of NiO films have yet to be investigated sufficiently. Moreover, designs of highly conductive doped carbon-embedded NiO films for multirole EC energy-storage electrodes has not been reported to date.

Herein, we report for the first time a unique design of N-doped carbon-embedded porous NiO films using a sol-gel method assisted by a multimeric amide condensation reaction, enabling the simultaneous construction of both N-doped carbon and a porous structure. Generated pores from the evaporated H₂O and embedded N-doped carbon effectively enhance EC energy-storage performance outcomes. This performance improvement was mainly attributed to the increased electrochemical activity caused by the porous surface morphology and the high electrical conductivity of the N-doped carbon embedded within the NiO films.

2. Experimental details

N-doped carbon-embedded NiO films with an optimized surface

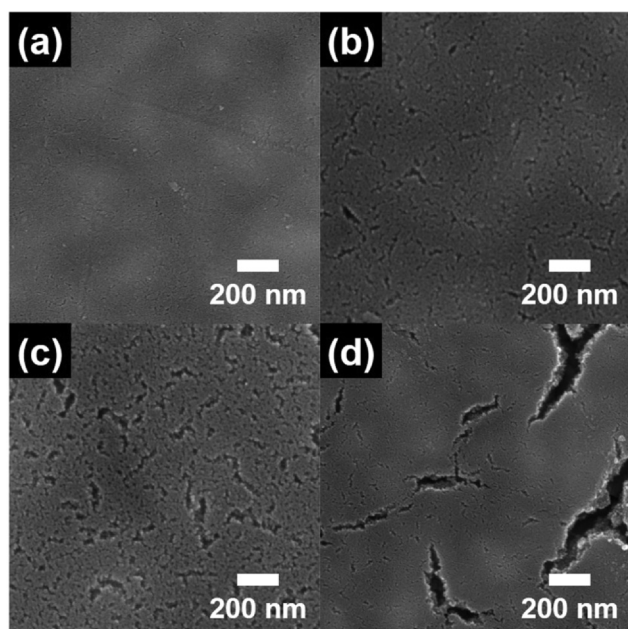


Fig. 2. Top-view FESEM images of (a) bare NiO, (b) 2.0OL-NiO, (c) 2.5OL-NiO and (d) 3.0OL-NiO samples.

pore structure were prepared using a spin-coating technique at room temperature. Prior to the coating process, commercial FTO substrates purchased from Pilkington ($8.0 \Omega/\square$) were consecutively cleaned in acetone, ethanol, and deionized water using ultrasonication. Initially, for the preparation of the sol solution, 0.5 M nickel chloride hexahydrate (Duksan) and citric acid (Aldrich) as the ligand-forming gelling agent were dissolved in pure ethanol (Duksan). After vigorous stirring in a chemical bath at 60°C for two hours, a set amount of oleylamine (Aldrich) was added to generate pores and the N-doped carbon structure by inducing a multimeric condensation reaction. In order to obtain the optimized surface pore structure, which is accompanied by the desired EC energy-storage performance, different amounts of oleylamine were added to the solution, in this case 2.0, 2.5, and 3.0 wt% of the solvent. After stirring for two hours at 30°C and maintaining these conditions for one hour under an ambient temperature, the resultant sol solutions were spin-coated at 2000 rpm for 30 s onto the prepared commercial FTO substrates. Thereafter, the respective samples were annealed at 300°C in air to obtain the EC energy-storage electrodes (thereafter identified as the bare NiO, 2.0OL-NiO, 2.5OL-NiO, 3.0OL-NiO samples, respectively).

To characterize the thermal behavior of the precursor solutions and the fabricated electrodes, thermogravimetric (TG, TGA-50) and differential scanning calorimetry (DSC-60, Shimadzu) measurements were carried out. The surface morphology of the samples was identified using field-emission scanning electron microscopy (FESEM, Hitachi S-4800). Structural and chemical bonding state analyses were done via X-ray diffraction measurements (XRD, Rigaku D/Max-2500 diffractometer using $\text{Cu K}\alpha$ radiation) and X-ray photoelectron spectroscopy measurements (XPS, ESCALAB 250 equipped with an $\text{Al K}\alpha$ X-ray source), respectively. The electrical and optical properties were correspondingly investigated by a Hall-effect measurement system (Ecopia, HMS-3000) and ultraviolet-visible (UV-vis) spectroscopy (Perkin-Elmer, Lambda-35). The electrochemical analysis was executed using a potentiostat/galvanostat (PGSTAT302N, FRA32M, Metrohm Autolab B.V., Netherlands), and electrochemical impedance spectroscopy (EIS) was used to evaluate the EC energy-storage performance capabilities. Measurements were conducted in a three-electrode electrochemical cell with 1 M KOH as the electrolyte. An Ag wire was used as a reference electrode, and Pt wire served as a counter electrode. Various scan rates

(20, 40, 60, 80, and 100 mV/s) were applied during the cyclic voltammetry assessment to calculate the diffusion coefficients of all samples. *In situ* optical properties to confirm the switching speed were measured using UV-vis spectroscopy at a wavelength of 450 nm.

3. Results and discussion

We synthesize N-doped carbon-embedded porous NiO films using the spin-coating method. Fig. 1a presents a schematic depiction of the unique synthetic procedure used simultaneously to construct both the N-doped carbon and porous structure on the NiO films by a consecutive amide condensation reaction. During the annealing process, the reaction between the carboxylic functional groups from citric acid and the amine functional groups from oleylamine begins at more than 130°C , producing a citric acid amide and an H_2O molecule [24]. As the temperature is then increased to 300°C , the formed citric acid amides condense to form the corresponding multimers, with these multimers then constructing the N-doped carbon structure. At this point, due to the evaporation of the H_2O stemming from the above reaction to induce shrinkage of the NiO films, the porous surface morphology is developed [25,26]. This eventual film structure with the N-doped carbon-embedded porous morphology can effectively contribute to the EC energy-storage performance by providing high electrochemical activity and electrical conductivity to the NiO films.

To confirm the mechanism of the N-doped carbon formation and pore generation within the films, DSC measurements of the precursor solutions with various amounts of oleylamine were conducted at $100\text{--}300^\circ\text{C}$ (see Fig. 1b). All precursor solutions demonstrated a gradual slope in the range of $225\text{--}260^\circ\text{C}$ according to the formation of the amorphous NiO structure. As the amount of oleylamine was increased from 0 to 3.0 wt%, the generated quantity of heat gradually increased. This behavior is mainly due to the exothermic nature of the multimeric amide condensation reaction between the carboxylic group of citric acid and the amine group of the added oleylamine [27]. As such, this heat flow escalation according to the amount of oleylamine can support the occurrence of amide condensation reactions and the further formation of N-doped carbon via citric acid amides. In an effort to verify the existence of the N-doped carbon within the porous NiO films, TGA measurements of all fabricated films were also taken. As shown in the inset of Fig. 1c, while there was no weight-loss tendency for the bare NiO, noticeable weight loss of the films using oleylamine was revealed at $400\text{--}500^\circ\text{C}$, which gradually stood out from the rates of 99.67% for the bare NiO to 98.25% for the 3.0OL-NiO samples. This result represents an increase in the amount of N-doped carbon existing within the films, as the evaporation temperature is reported to be in the range of $400\text{--}500^\circ\text{C}$ [28].

Fig. 2a–d show top-view FESEM images of the bare NiO, 2.0OL-NiO, 2.5OL-NiO, and 3.0OL-NiO samples, respectively. For the bare NiO (see Fig. 2a), a smooth and dense surface morphology appears to have formed. This implies the construction of typical amorphous NiO films as compared to the formation of the plate-type morphology typically associated with crystalline NiO films. In contrast, the 2.0OL-NiO and 2.5OL-NiO samples (see Fig. 2b–c) showed a porous surface morphology of sturdy films, in which the distribution and size of the formed pores gradually improved with an increase of the oleylamine amount from 2.0 wt% to 2.5 wt% owing to the evaporation of H_2O stemming from the amide condensation reaction between the citric acid and the oleylamine (see Table S1) [29,30]. This porous surface morphology can contribute to the enhancement of the EC energy-storage performance by providing extra active sites and shortening the ion diffusion length during the electrochemical reactions. However, when the amount of oleylamine reaches 3.0 wt% (see Fig. 2d), a discontinuous film structure with nonuniform pore sizes forms as this amount of oleylamine induces excessive H_2O evaporation. The erratic surface morphology in this case brings about an increase in the electrochemical resistance caused by the indiscreet distance with the film matrix, which can degrade the

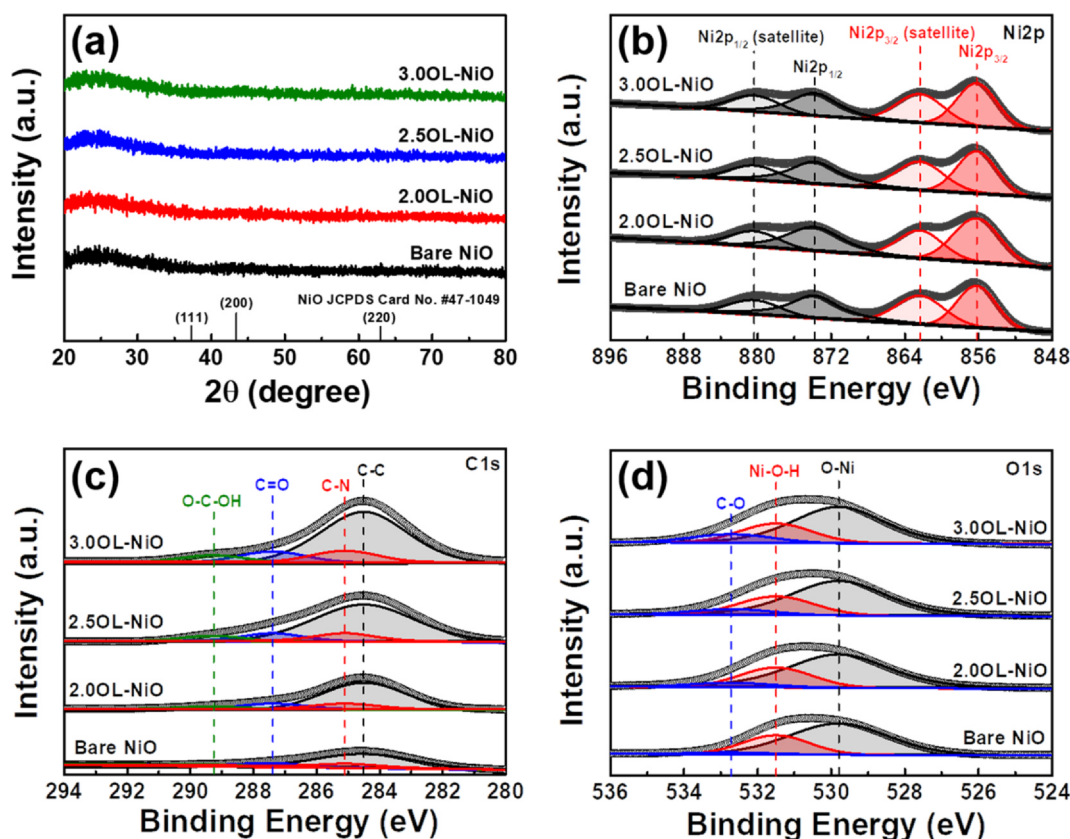


Fig. 3. (a) XRD curves and XPS core-level spectra of (b) Ni 2p, (c) C 1s, and (d) O 1s obtained from bare NiO, 2.0OL-NiO, 2.5OL-NiO, and 3.0OL-NiO samples.

electrochemical activity [31]. Moreover, the 2.5OL-NiO displays the increased distribution of carbon atoms generated from amide condensation reaction compared to the bare NiO by using EDS analysis (see Fig. S3). Thus, the 2.5OL-NiO sample showed an optimized porous film structure with numerous active sites, which contributes to the electrochemical activity.

Fig. 3a shows the XRD curves of all films, assessed to analyze their crystal structure. All curves exhibit a broad diffraction peak that corresponds to amorphous NiO films, potentially offering kinetic advantages with regard to the switching speed and coloration efficiency due to the rapid ion transfer through the open structure [15]. In addition, no discernible peaks related to carbon were observed on the fabricated films due to the relatively low synthetic energy required to form the crystal structure [32]. Therefore, we took XPS measurements to characterize the chemical bonding states of the fabricated films (see Fig. 3b–d). All binding energy levels of the samples were arranged according to shift of C 1s to 284.5 eV as a reference. Fig. 3b exhibits the Ni 2p XPS core-level spectra, showing that all fabricated samples possessed two pairs of doublets at 873.8 eV for Ni 2p_{1/2} and 880.4 eV for Ni 2p_{1/2} (satellite), and at 856.2 eV for Ni 2p_{3/2} and 862.3 eV for Ni 2p_{3/2} (satellite). The successful formation of the NiO phase was confirmed through these results, and constant chemical bonding states were observed as the amount of oleylamine was increased [33,34]. Otherwise, apparent differences in the detected intensity levels were observed among the samples in the core-level spectra of C 1s (see Fig. 3c). The summarized C 1s XPS curves were divided into four peaks associated with C–C bonding of 284.5 eV, C–N bonding of 285.1 eV, C=O bonding of 287.4 eV, and O–C–OH bonding of 289.2 eV. At the bare NiO, only broad and weak C–C bonding types were noted. However, extra peaks of C–N, C=O, O–C–OH bonds were confirmed for the other films with oleylamine, in which the area ratios of carbon-related bonds to O–Ni bonds were gradually increased from 10.3% to 38.56% with an increase in the amount of oleylamine (see Table S2), while

keeping the area ratio of C–N/C–C constant. In addition, the core-level spectra of O 1s (see Fig. 3d) also demonstrated an increased trend of carbon-related bonding (O–C bonding at 532.7 eV) compared to the commonly detected O–Ni bond at 529.8 eV and the detected Ni–O–H bond at 531.5 eV. There results confirm an increased amount of N-doped carbon with a constant N-doping ratio within the fabricated films as the amount of oleylamine was increased [35,36]. Due to the high conductivity of N-doped carbon, this N-doped carbon-embedded construction with NiO films can effectively accelerate the switching speeds via a preferred electron pathway [37].

To evaluate the electrical and optical properties of the N-doped carbon-embedded NiO films with various amounts of oleylamine, all samples were identically coated onto glass substrates (Corning, Eagle XG™). The electrical conductivity was characterized using a Hall-effect measurement system (Ecopia, HMS-3000). Fig. 4a depicts the increasing trend, i.e., from the bare NiO at 3.98×10^{-6} S/cm to the 2.0OL-NiO sample at 4.33×10^{-6} S/cm and to the 2.5OL-NiO sample at 4.55×10^{-6} S/cm. This outcome is mainly attributed to the high electrical conductivity of the N-doped carbon compared to the NiO films, providing a favored electron pathway within the films. In contrast, the electrical conductivity of the 3.0OL-NiO sample decreased (4.43×10^{-6} S/cm) despite the largest amount of oleylamine. This result confirms that an excessive amount of oleylamine can be assumed to generate a discontinuous film surface with wide cracks, as shown in the top-view SEM image in Fig. 2. Subsequently, Tauc plots of all films were produced to calculate their bandgap energy levels, as shown in Fig. 4b. These plots represent the excitation of electrons between the valence band and the conduction band. The calculation was done using Eq. (1) [18,38]:

$$(\alpha h\nu)^{1/n} = A(h\nu - E_g) \quad (1)$$

The interrelation between the absorption coefficient (α) and the incident photon energy ($h\nu$) is also determined with the above equation,

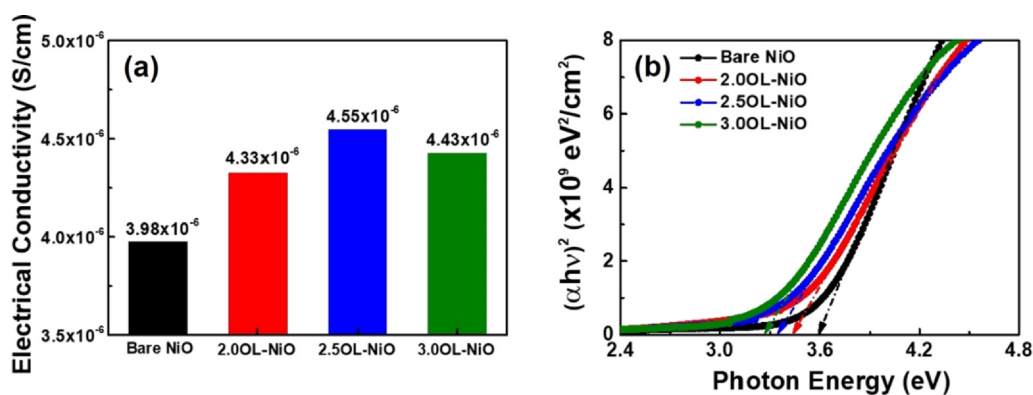
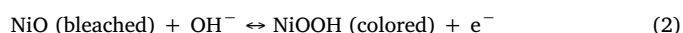


Fig. 4. (a) Electrical conductivity and (b) band gap energy of bare NiO, 2.0OL-NiO, 2.5OL-NiO, and 3.0OL-NiO samples measured in the wavelength range of 200 to 800 nm.

where n is the transition type, A is a constant, and E_g is the bandgap energy. After fitting the linear region of the spectra (see the dotted lines, which were extrapolated to the x -axis), the direct bandgap was determined. The bare NiO films showed bandgap energy of 3.60 eV, in good agreement with the values of NiO films reported in the literature [39,40]. Moreover, as the oleylamine was added to the sol solution, the bandgap energy decreased to 3.43 eV for the 2.0OL-NiO sample, to 3.34 eV for the 2.5OL-NiO sample, and to 3.26 eV for the 3.0OL-NiO sample. This bandgap-narrowing effect can be attributed to the increased amount of embedded N-doped carbon with the low bandgap energy (~ 2.5 eV) in the NiO films compared to that of the bare NiO [41]. Therefore, the effects of the added oleylamine on the electrical and optical properties of fabricated films were successfully analyzed and, as a result, the 2.5OL-NiO sample was found to exhibit the highest electrical conductivity among all films, showing an accelerated impact during electron transfers for an improvement of the EC energy performance.

To compare the electrochemical behavior of the samples, cyclic voltammetry (CV) measurements were carried out during the EC reaction using a three-electrode system. Fig. 5a displays the CV curves of the

samples in 1 M KOH electrolyte with the potential region ranging from 0 to 0.55 V (vs. Ag wire) at a 20 mV/s scan rate. Only one pair of redox peaks was observed for all samples, and each anodic/cathodic peak is indicative of the conversion reaction between the pale yellow NiO and the deep brown NiOOH, accompanied by OH^- intercalation/deintercalation and electron transportation. The reaction involved can be expressed as shown below in Eq. (2) [17,23]:



The current densities of the anodic and cathodic peaks were gradually increased from the bare NiO to the 2.5OL-NiO sample. This result is due to the increased pore distribution in the film structure, which signifies an improvement in the electrochemical activity to induce increased numbers of participated electrons and ions during the reaction. However, the 3.0OL-NiO sample showed a slight reduction in the peak current density, as expected from the abovementioned SEM image of the discontinuous and nonuniform surface morphology. Furthermore, to determine the ion diffusion coefficient during the electrochemical reaction, CV measurements of all films at various scan rates (20, 40, 60, 80, and 100 mV/s) were taken (see Fig. S2). The Randles-Sevcik

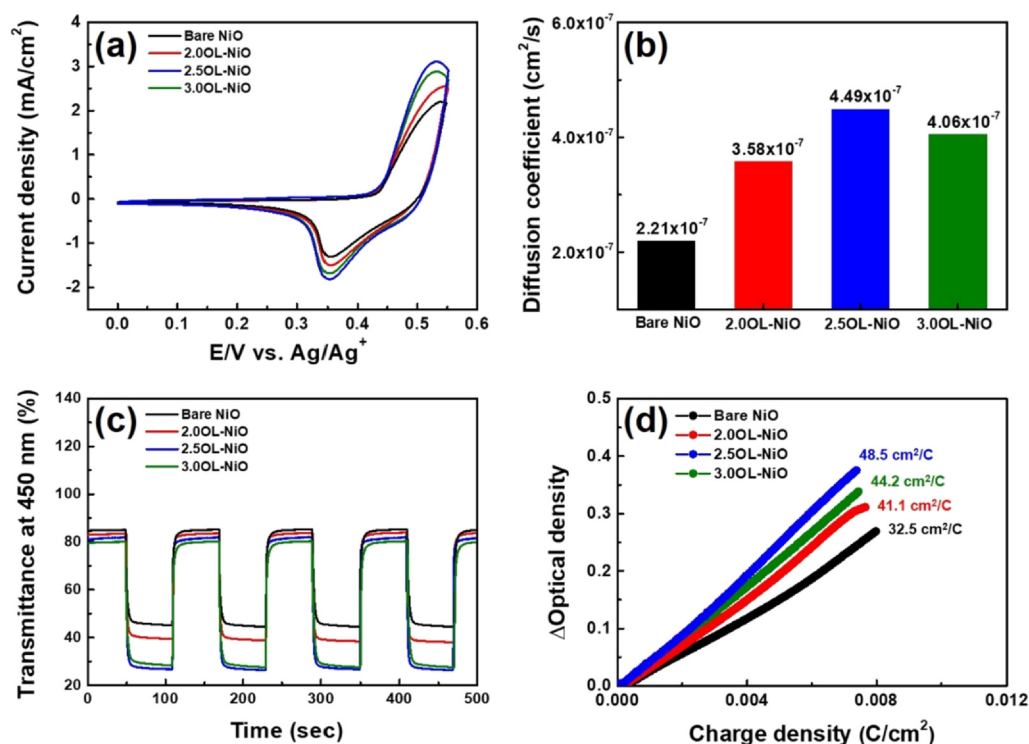


Fig. 5. (a) CV curves of the fabricated films recorded between 0.0 and 0.55 V at a scan rate of 20 mV/s using the three-electrode system, (b) calculated diffusion coefficient from the Randles-Sevcik equation, (c) *in situ* optical transmittance curves traced at a stepping potential of 0.0 V for the bleached state and 0.55 V for the colored state for 60 s, and (d) optical density variation at 450 nm with respect to the inserted charge density.

equation (Eq. (3)) was used to calculate the ion diffusion coefficient by considering the variation of the peak current density [30,42],

$$J_p = 2.72 \times 10^5 \times D^{1/2} \times C_o \times \nu^{1/2}, \quad (3)$$

where J_p , C_o , and ν are the peak current density, the active ion concentration of the electrolyte and the CV profiling scan rate, respectively. Fig. 5b shows the calculated Li-ion diffusion coefficients of all films, which were enhanced from $2.21 \times 10^{-7} \text{ cm}^2/\text{s}$ for the bare NiO, to $3.58 \times 10^{-7} \text{ cm}^2/\text{s}$ for the 2.0OL-NiO sample, and to $4.49 \times 10^{-7} \text{ cm}^2/\text{s}$ for the 2.5OL-NiO sample. The improvement in the electrical conductivity from the embedded N-doped carbon and the shortened ion diffusion length from the porous film structure generated from the added oleylamine area the main factors in this result [43]. Despite the largest amount of oleylamine used, the 3.0OL-NiO sample showed a lower Li-ion diffusion coefficient ($4.06 \times 10^{-7} \text{ cm}^2/\text{s}$) compared to the 2.5OL-NiO sample due to the discontinuous film surface with inferior electrical conductivity. Subsequently, the *in-situ* transmittance at 450 nm was observed during the redox reaction of the fabricated films to evaluate the transmittance response to voltage variations. Fig. 5c displays the *in-situ* transmittance curves of all samples after applying repeated stepped potentials of 0 V (bleached state) and 0.55 V (colored state) for 60 s. As summarized in Table 1, the transmittance modulation (transmittance variation between the colored state (T_c) and bleached state (T_b), ΔT) and the switching speed (response time to reach 90% of the transmittance modulation) were confirmed. In this case, the 2.5OL-NiO sample exhibited transmittance modulation up to 54.72%, 14.2% higher than that of the bare NiO due to the reduced transmittance value in the colored state caused by the enhanced electrochemical activity via a synergistic effect with the optimized porous morphology and electrical conductivity to accelerate the intercalation of OH^- into the NiO films. Moreover, obviously shortened switching speeds were observed from the 2.5OL-NiO sample (3.2 s for the coloration and 2.7 s for the bleaching speed) in comparison with the bare NiO (9.3 s for the coloration and 8.8 s for the bleaching speed). This enhancement of the switching speed is closely associated with the high conductivity of the embedded N-doped carbon, which facilitates electron and Li-ion transport within the films as voltage is applied. However, the discontinuous film morphology due to the excessive amount of oleylamine (3.0OL-NiO samples) interrupted the electron and ion transport and caused a decrement of the switching speeds (5.0 s for the coloration and 3.8 s for the bleaching speed). The CE values of all samples were also calculated (see Fig. 5d) as a main factor that briefly represents the comprehensive EC performance using Eqs. (4) and (5) [44,45] below:

$$\text{CE} = \Delta\text{OD}/(Q/A) \quad (4)$$

$$\Delta\text{OD} = \log(T_b/T_c) \quad (5)$$

Given that the CE value is determined by the optical density (OD) variation according to the inserted charge per area (Q/A), considerable transmittance modulation with a definite charge amount is important to achieve high CE value. The CE values were $32.5 \text{ cm}^2/\text{C}$ for the bare NiO, $41.1 \text{ cm}^2/\text{C}$ for the 2.0OL-NiO sample, $48.5 \text{ cm}^2/\text{C}$ for the 2.5OL-NiO sample, and $44.2 \text{ cm}^2/\text{C}$ for the 3.0OL-NiO sample, indicating that the 2.5OL-NiO sample exhibited optimized EC performance. This outcome is mainly due to the large transmittance modulation with low charge consumption caused by the porous surface morphology, which provides sufficient electrochemical reaction sites.

Table 1
Summary of EC performances measured from all samples.

Samples	Wavelength (nm)	T_b (%)	T_c (%)	Transmittance modulation (%)	Coloration speed (s)	Bleaching speed (s)	CE (cm^2/C)
Bare NiO	450	85.30	44.78	40.52	9.3	8.8	32.5
2.0OL-NiO	450	83.73	38.83	44.90	6.8	4.0	41.1
2.5OL-NiO	450	81.98	27.26	54.72	3.2	2.7	48.5
3.0OL-NiO	450	80.12	27.88	52.24	5.0	3.8	44.2

Fig. 6a presents the galvanostatic charge/discharge curves between the bare NiO and the 2.5OL-NiO sample to demonstrate the capacitance performance at the current density of 2 A/g. Each sample shows one pair of charge/discharge curves, and the 2.4OL-NiO sample exhibits a much longer discharging time compared to that of the bare NiO, which signifies abundant electrochemical active sites with a porous surface morphology. The specific capacitances (C_{sp}) with various current densities (2, 4, 6, 8, and 10 A/g) were also determined using Eq. (6) [46,47] below:

$$C_{sp} = 4I/(m\text{dV}/dt) \quad (6)$$

Fig. 6b shows the summarized specific capacitance values of the bare NiO and 2.5OL-NiO samples. As expected, the 2.5OL-NiO sample exhibited a much higher specific capacitance value (235.8 F/g at the current density of 2 A/g) in comparison with bare NiO (159.4 F/g at the current density of 2 A/g). Along with the increase of the sample current density to 10 A/g, the 2.5OL-NiO sample demonstrated superior rate capability (75.9% compared to 2 A/g) relative to that of the bare NiO sample (43.9% compared to 2 A/g). This is due to the facilitated electrochemical kinetics with a shortened Li-ion diffusion length according to the porous film morphology. To confirm the high electrical conductivity and Li-ion diffusion coefficient of the N-doped carbon-embedded NiO films, EIS measurements of all films were taken. The equivalent circuit model is shown in the inset of Fig. 7, consisting of R_s (a combination of the electrolyte resistance, intrinsic resistance of the active materials, and the interface contact resistance with the active materials and current collectors), R_{ct} (charge transfer resistance), Z_w (Warburg resistance), C_{dl} (double-layer capacitance), and C_{ps} (pseudo-capacitance). Nyquist plots of all films (see Fig. 7) showed a single semicircle in the high-frequency zone and an inclined line in the low-frequency zone. These semicircles and lines reflect the inner resistance of the electrode and the ionic diffusion rate within the electrode, respectively [48]. The 2.5OL-NiO sample showed the smallest semicircle in the high-frequency zone and the highest slope of the inclined line in the low-frequency zone among all films. This result demonstrates that the 2.5OL-NiO films possess high electrical conductivity and a high ionic diffusion rate due to the embedded N-doped carbon and porous surface morphology.

Thus, the superior electrochemical performance of the N-doped carbon-embedded NiO can be attributed to the optimized surface pore structure and high electrical conductivity of N-doped carbon compared to those of NiO. First, the optimized surface pore structure effectively enhanced the electrochemical activity, which can directly affect the EC transmittance modulation with CE and the energy-storage performance. Secondly, the high electrical conductivity of the embedded N-doped carbon successfully contributed to the reduction of the switching speeds. Therefore, the use of N-doped carbon-embedded NiO with enhanced electrochemical performance suggests an interesting opportunity to develop multirole EC energy-storage devices.

4. Conclusion

In summary, we successfully demonstrated multirole EC energy-storage electrodes with N-doped carbon-embedded NiO films. The citric acid sol solution and added oleylamine as used here generated citric acid amide, which forms an N-doped carbon structure through a

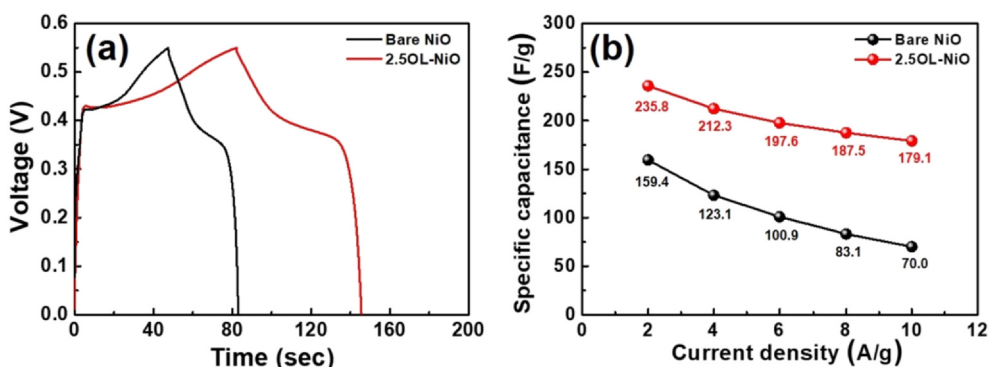


Fig. 6. (a) Comparison of galvanostatic charge/discharge curves between bare NiO and 2.5OL-NiO measured at scan rates of 2 A/g in the potential range from 0.0 to 0.55 V and (b) specific capacitance as a function of the current density.

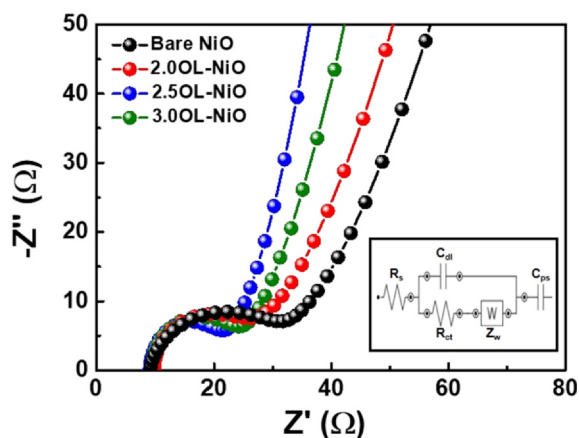


Fig. 7. Nyquist plots of the EIS obtained from bare NiO, 2.0OL-NiO, 2.5OL-NiO, and 3.0OL-NiO.

multimeric condensation reaction. It should be noted that the water molecules obtained from this reaction developed the surface pore structure by evaporation during the annealing process, and the N-doped carbon which formed enhanced the electrical conductivity of the films. Therefore, the 2.5OL-NiO sample showed optimized EC performance outcomes, including the switching speed (3.2 s for the coloration speed and 2.7 s for the bleaching speed) and a large transmittance modulation rate of 54.72% with a CE value of 48.5 cm²/C. Furthermore, the 2.5OL-NiO sample showed high specific capacitance (235.8 F/g at a current density of 2 A/g) with superior rate capability (75.9% compared to 2 A/g). This improvement of the electrochemical performance was mainly due to the (1) high electrochemical activity of the porous surface morphology, and (2) the high electrical conductivity of the embedded N-doped carbon. In conclusion, these findings are promising because N-doped carbon-embedded NiO electrodes hold great potential for use in multirole EC energy-storage devices.

CRediT authorship contribution statement

Kue-Ho Kim: Conceptualization, Methodology, Investigation, Writing - original draft. **Seock-Joon Jeong:** Methodology. **Bon-Ryul Koo:** Methodology. **Hyo-Jin Ahn:** Conceptualization, Supervision, Writing - review & editing.

Declaration of Competing Interest

The authors declare that they have no known competing financial interests or personal relationships that could have appeared to influence the work reported in this paper.

Acknowledgements

This work was supported by the National Research Foundation of Korea (NRF) grant funded by the Korea government (MSIT) (No. 2019R1 A2 C1005836).

Appendix A. Supplementary material

Supplementary data to this article can be found online at <https://doi.org/10.1016/j.apsusc.2020.147902>.

References

- [1] M. Grätzel, Ultrafast colour displays, *Nature* 409 (2001) 575–576.
- [2] P. Salles, D. Pinto, K. Hantanasirisakul, K. Maleski, C.E. Shuck, Y. Gogotsi, Electrochromic effect in titanium carbide MXene thin films produced by dip-coating, *Adv. Func. Mater.* 29 (2019) 1809223.
- [3] Q. Zhang, C.-Y. Tsai, L.-J. Li, D.-J. Liaw, Colorless-to-colorful switching electrochromic polyimides with very high contrast ratio, *Nat. Commun.* 10 (2019) 1–8.
- [4] T. Yun, M. Park, D.-H. Kim, D. Kim, J. Cheong, J. Bae, S. Han, I.-D. Kim, All-transparent stretchable electrochromic supercapacitor wearable patch device, *ACE Nano* 13 (2019) 3141–3150.
- [5] S. Zhang, S. Cao, T. Zhang, A. Fisher, J. Lee, Al³⁺ intercalation/de-intercalation-enabled dual-band electrochromic smart windows with a high optical modulation, quick response and long cycle life, *Energy Environ. Sci.* 11 (2018) 2884–2892.
- [6] K. Shen, K. Sheng, Z. Wang, J. Zheng, C. Xu, Cobalt ions doped tungsten oxide nanowires achieved vertically aligned nanostructure with enhanced electrochromic properties, *Appl. Surf. Sci.* 501 (2020) 144003.
- [7] W. Shen, X. Huo, M. Zhang, M. Guo, Synthesis of oriented core/shell hexagonal tungsten oxide/amorphous titanium dioxide nanorod arrays and its electrochromic-pseudocapacitive properties, *Appl. Surf. Sci.* 515 (2020) 146034.
- [8] B.-R. Koo, M.-H. Jo, K.-H. Kim, H.-J. Ahn, Multifunctional electrochromic energy storage devices by chemical cross-linking: impact of a WO₃·H₂O nanoparticle-embedded chitosan thin film on amorphous WO₃ films, *NPG Asia Mater.* 12 (2020) 10.
- [9] B.-R. Koo, H.-J. Ahn, Fast-switching electrochromic properties of mesoporous WO₃ films with oxygen vacancy defects, *Nanoscale* 9 (2017) 17788–17793.
- [10] G. Cai, J. Wang, P. Lee, Next-generation multifunctional electrochromic devices, *Acc. Chem. Res.* 49 (2016) 1469–1476.
- [11] J. Matsui, R. Kikuchi, T. Miyashita, A trilayer film approach to multicolor electrochromism, *J. Am. Chem. Soc.* 136 (2014) 842–845.
- [12] N. Vuong, D. Kim, H. Kim, Electrochromic properties of porous WO₃-TiO₂ core-shell nanowires, *J. Mater. Chem. C* 1 (2013) 3399–3407.
- [13] S. Pereira, A. Goncalves, N. Correia, J. Pinto, L. Pereira, R. Martins, E. Fortunato, Electrochromic behavior of NiO thin films deposited by e-beam evaporation at room temperature, *Sol. Energy Mater. Sol. Cells* 120 (2014) 109–115.
- [14] G. Niklasson, C. Granqvist, Electrochromics for smart windows: thin films of tungsten oxide and nickel oxide, and devices based on these, *J. Mater. Chem.* 17 (2007) 127–156.
- [15] A.I. Inamdar, A.C. Sonavane, S.M. Pawar, Y.-S. Kim, J.-H. Kim, P.S. Patil, W. Jung, H.-S. Im, D.-Y. Kim, H.-S. Kim, Electrochromic and electrochemical properties of amorphous porous nickel hydroxide thin films, *Appl. Surf. Sci.* 257 (2011) 9606–9611.
- [16] Y. Ghalimi, F. Habelhames, A. Sayah, A. Bahloul, B. Nessark, M. Shalabi, J.M. Nunzi, Capacitance performance of NiO thin films synthesized by direct and pulse potentiostatic methods, *Ionics* 25 (2019) 6025–6033.
- [17] J. Zhang, G. Cai, D. Zhou, H. Tang, X. Wang, C. Gu, J. Tu, Co-doped NiO nanoflake array films with enhanced electrochromic properties, *J. Mater. Chem. C* 2 (2014) 7013–7021.
- [18] B.-R. Koo, K.-H. Kim, H.-J. Ahn, Switching electrochromic performance improvement enabled by highly developed mesopores and oxygen vacancy defects of Fe-

- doped WO₃ films, *Appl. Surf. Sci.* 453 (2018) 238–244.
- [19] J.Z. Ou, S. Balendran, M.R. Field, D.G. McCulloch, A.S. Zoofakar, R.A. Rani, S. Zhuiykov, A.P. O'Mullane, K. Kalantar-zadeh, The anodized crystalline WO₃ nanoporous network with enhanced electrochromic properties, *Nanoscale* 4 (2012) 5980–5988.
- [20] S.R. Bathe, P.S. Patil, Electrochromic characteristics of fibrous reticulated WO₃ thin films prepared by pulsed spray pyrolysis technique, *Sol. Energy Mater. Sol. Cells* 91 (2007) 1097–1101.
- [21] X. Yang, G. Zhu, S. Wang, R. Zhang, L. Lin, W. Wu, Z.L. Wang, A self-powered electrochromic device driven by a nanogenerator, *Energy Environ. Sci.* 5 (2012) 9462–9466.
- [22] X.H. Xia, J.P. Tu, J. Zhang, X.L. Wang, W.K. Zhang, H. Huang, Electrochromic properties of porous NiO thin films prepared by a chemical bath deposition, *Sol. Energy Mater. Sol. Cells* 92 (2008) 628–633.
- [23] Y. Chen, Y. Wang, P. Sun, P. Yang, L. Du, W. Mai, Nickel oxide nanoflake-based bifunctional glass electrodes with superior cyclic stability for energy storage and electrochromic applications, *J. Mater. Chem. A* 3 (2015) 20614–20618.
- [24] T. Ogi, K. Aishima, F.A. Permatasari, F. Iskandar, E. Tanabe, K. Okuyama, Kinetics of nitrogen-doped carbon dot formation via hydrothermal synthesis, *New J. Chem.* 40 (2016) 5555–5561.
- [25] L. Zhu, Z. Wen, W. Mei, Y. Li, Z. Ye, Porous CoO Nanostructure Arrays Converted from Rhombic Co(OH)F and Needle-like Co(CO₃)_{0.5}(OH)·0.11H₂O and Their Electrochemical Properties, *J. Phys. Chem.* 117 (2013) 20465–20473.
- [26] T.S. Tan, H.Y. Chin, M.-L. Tsai, C.-L. Liu, Structural alterations, pore generation, and deacetylation of α - and β -chitin submitted to steam explosion, *Carbohydr. Polym.* 122 (2015) 321–328.
- [27] J.C. Neves, V.G. Castro, A.L.S. Assis, A.G. Veiga, M.L.M. Rocco, G.G. Silva, In-situ determination of amine/epoxy and carboxylic/epoxy exothermic heat of reaction on surface of modified carbon nanotubes and structural verification of covalent bond formation, *Appl. Surf. Sci.* 436 (2018) 495–504.
- [28] M. Xu, S. Xu, Z. Yang, M. Shu, G. He, D. Huang, L. Zhang, L. Li, D. Cui, Y. Zhang, Hydrophilic and blue fluorescent N-doped carbon dots from tartaric acid and various alkylol amines under microwave irradiation, *Nanoscale* 7 (2015) 15915–15923.
- [29] W. Niu, S. Wu, S. Zhang, Utilizing the amidation reaction to address the “co-operative effect” of carboxylic acid/amine on the size, shape, and multicolor output of fluoride upconversion nanoparticles, *J. Mater. Chem.* 21 (2011) 10894–10902.
- [30] M.A. Hubbe, O.J. Rojas, L.A. Lucia, Green modification of surface characteristics of cellulosic materials at the molecular or nano scale: a review, *BioResources* 10 (2015) 6095–6206.
- [31] B.-R. Koo, K.-H. Kim, H.-J. Ahn, Novel tunneled phosphorus-doped WO₃ films achieved by ignited red phosphorus for stable and fast switching electrochromic performances, *Nanoscale* 11 (2019) 3318–3325.
- [32] N. Puvvada, B.N.P. Kumar, S. Konar, H. Kalita, M. Mandal, A. Pathak, Synthesis of biocompatible multicolor luminescent carbon dots for bioimaging applications, *Sci. Technol. Adv. Mater.* 13 (2012) 045008.
- [33] T. Liu, L. Zhang, B. Cheng, W. You, J. Yu, Fabrication of a hierarchical NiO/C hollow sphere composite and its enhanced supercapacitor performance, *Chem. Commun.* 54 (2018) 3731–3734.
- [34] Q. Dong, C. Sun, Z. Dai, X. Zang, X. Dong, Free-standing NiO@C nanobelt as an efficient catalyst for water splitting, *Chem. Cat. Chem.* 8 (2016) 1–7.
- [35] Z. Li, H. Yu, T. Bian, Y. Zhao, C. Zhou, L. Shang, Y. Liu, L.-Z. Wu, C.-H. Tung, T. Zhang, Highly luminescent nitrogen-doped carbon quantum dots as effective fluorescent probes for mercuric and iodide ions, *J. Mater. Chem. C* 3 (2015) 1922–1928.
- [36] H. Wang, P. Sun, S. Cong, J. Wu, L. Gao, Y. Wang, X. Dai, Q. Yi, G. Zou, Nitrogen-doped carbon dots for “green” quantum dot solar cells, *Nanoscale Res. Lett.* 11 (2016) 27.
- [37] L. Marcinauskas, Z. Kavaliauskas, V. Valincius, Carbon and nickel oxide/carbon composites as electrodes for supercapacitors, *J. Mater. Sci.* 28 (2012) 931–936.
- [38] S. Shanthi, C. Subramanian, P. Ramasamy, Investigations on the optical properties of undoped, fluorine doped and antimony doped tin oxide films, *Cryst. Res. Technol.* 34 (1999) 1037–1046.
- [39] S.D. Singh, A. Das, R.S. Ajimsha, M.N. Singh, A. Upadhyay, R. Kamparath, C. Mukherjee, P. Misra, S.K. Rai, A.K. Sinha, T. Ganguli, Studies on structural and optical properties of pulsed laser deposited NiO thin films under varying deposition parameters, *Mater. Sci. Semicond. Process* 66 (2017) 186–190.
- [40] N.S. Das, B. Saha, R. Thapa, G.C. Das, K.K. Chattopadhyay, Band gap widening of nanocrystalline nickel oxide thin films via phosphorus doping, *Physica E* 42 (2010) 1377–1382.
- [41] D. Carolan, C. Rocks, D.B. Padmanaban, P. Maguire, V. Svrcek, D. Mariotti, Environmentally friendly nitrogen-doped carbon quantum dots for next generation solar cells, *Sustain. Energy. Fuels* 1 (2017) 1611–1619.
- [42] H. Kim, D. Choi, K. Kim, W. Chu, D.-M. Chun, C.S. Lee, Effect of particle size and amorphous phase on the electrochromic properties of kinetically deposited WO₃ films, *Sol. Energy Mater. Sol. Cells* 177 (2018) 44–50.
- [43] G. Yuan, C. Hua, D. Khan, S. Jiang, Z. Wu, Y. Liu, J. Wang, C. Song, G. Han, *Electrochim. Acta* 260 (2018) 274–280.
- [44] A. Zhou, X. Liu, Y. Dou, S. Guan, J. Han, M. Wei, The fabrication of oriented organic-inorganic ultrathin films with enhanced electrochromic properties, *J. Mater. Chem. C* 4 (2016) 8284–8290.
- [45] G. Cai, M. Cui, V. Kumar, P. Darmawan, J. Wang, X. Wang, A.L.-S. Eh, K. Qian, P.S. Lee, Ultra-large optical modulation of electrochromic porous WO₃ film and the local monitoring of redox activity, *Chem. Sci.* 7 (2016) 1373–1382.
- [46] K.-H. Kim, D.-Y. Shin, H.-J. Ahn, Ecklonia cava based mesoporous activated carbon for high-rate energy storage devices, *J. Ind. Eng. Chem.* 84 (2020) 393–399.
- [47] M. Amiri, S.S.H. Davarani, S.K. Kaverlavani, S.E. Moosavifard, M. Shamsipur, Construction of hierarchical nanoporous CuCo₂V₂O₈ hollow spheres as a novel electrode material for high-performance asymmetric supercapacitors, *Appl. Surf. Sci.* 527 (2020) 146855.
- [48] J. Li, W. Zhao, F. Huang, A. Manivannan, N. Wu, Single-crystalline Ni(OH)₂ and NiO nanoplatelet arrays as supercapacitor electrodes, *Nanoscale* 3 (2011) 5103–5109.